Fluorescence self-quenching from reporter dyes informs on the structural properties of amyloid clusters formed *in vitro* and in cells

WeiYue Chen[1], Laurence J. Young[1], Meng Lu[1], Alessio Zaccone[1], Florian Ströhl[1], Na Yu[1], Gabriele S. Kaminski Schierle[1], Clemens F. Kaminski[1]*

[1]Department of Chemical Engineering and Biotechnology, University of Cambridge, Pembroke Street, Cambridge CB2 3RA, United Kingdom

ABSTRACT The characterization of the aggregation kinetics of protein amyloids and the structural properties of the ensuing aggregates are vital in the study of the pathogenesis of many neurodegenerative diseases and the discovery of therapeutic targets. In this article, we show that the fluorescence lifetime of synthetic dyes covalently attached to amyloid proteins informs on the structural properties of amyloid clusters formed both *in vitro* and in cells. We demonstrate that the mechanism behind such a "lifetime sensor" of protein aggregation is based on fluorescence self-quenching, and that it offers a good dynamic range to report on various stages of aggregation without significantly perturbing the process under investigation. We show that the sensor informs on the structural density of amyloid clusters in a high-throughput and quantitative manner and in these aspects the sensor outperforms super-resolution imaging techniques. We

1

demonstrate the power and speed of the method, offering capabilities for example in therapeutic screenings that monitor biological self-assembly. We investigate the mechanism and advantages of the lifetime sensor in studies of the K18 protein fragment of the Alzheimer's disease related protein tau and its amyloid aggregates formed *in vitro*. Finally, we demonstrate the sensor in the study of aggregates of polyglutamine (polyQ) protein, a model used in studies related to Huntington's disease, by performing correlative fluorescence lifetime imaging microscopy (FLIM) and structured-illumination microscopy (SIM) experiments in cells.

Protein misfolding and aggregation has been linked to many neurodegenerative diseases including Alzheimer's disease (AD), Parkinson's disease (PD), and Huntington's disease (HD). A capability of monitoring amyloid protein aggregation both *in vitro* and in cells is vital for gaining further insights into the pathogenesis of, and to discover therapeutic strategies for, such disorders [1-6]. Previous work has suggested that amyloid clusters formed under different environmental conditions are morphologically distinct, and that the structural properties of aggregates are linked to disease pathology[7-12]. A structural characterization of amyloid clusters is thus an important topic of research in the field. Various approaches have been employed to reveal the morphology of individual amyloid fibrils or clusters directly, for instance electron microscopy (EM)[2, 5, 8, 12, 13], atomic-force microscopy (AFM)[11, 12, 14-16] and super-resolution fluorescence microscopy[17-22]. However, such methods are slow to perform and can require elaborate sample preparation protocols, making them impractical to perform for screening applications or the analysis of large data sets. There are also limitations with these techniques in their applicability for studies in biological systems. For these reasons a high-throughput method,

which offers structural information of amyloid clusters and that is suitable for studies of protein aggregation both *in vitro* and in cells, is highly desirable.

Fluorescence imaging of proteins labelled covalently with synthetic organic fluorophores has proven to be a powerful method to study amyloid aggregation both *in vitro* and in cells[7, 14, 18, 23, 24]. It informs on amyloid formation either by direct observation of the morphology of amyloid deposits *via* super-resolution microscopy, or, indirectly, *via* changes in spectroscopic properties, such as the fluorescence intensity or lifetime. The fluorescence lifetime is particularly important in this respect, as it is an inherently ratiometric technique and thus less prone to concentration and intensity artefacts[25, 26]. Fluorescence lifetime imaging microscopy (FLIM) has previously been used on covalently labelled amyloid proteins to report on amyloid aggregation[7, 18, 23, 24]. One of these methods requires only a single color as label[18, 23, 24], and holds great promise as a practical and powerful reporter for structural transformations of amyloid protein. However, to date the mechanism of lifetime changes in the reporter fluorophores upon aggregation has not been adequately elucidated. Furthermore, there have been no attempts to correlate lifetime values to underlying amyloid structure, and reported applications have so far been qualitative rather than quantitative in nature.

In this paper, we demonstrate that the fluorescence lifetime of synthetic dyes covalently attached to amyloid proteins informs on the density and morphological properties of amyloid clusters, and conclude that this is affected by fluorescence self-quenching of the dye molecules upon aggregation. The method requires only a single type of fluorescent dye to label the protein of interest. In what follows we refer to this concept as "lifetime sensor" for amyloid aggregation. We show that the lifetime sensor enables the probing of the structural density of amyloid clusters in a high-throughput manner, with negligible influence on the kinetics of aggregation. We

demonstrate the method both *in vitro* and in cells, *via* FLIM and optical sectioning structured-illumination microscopy (SROS-SIM) measurements of amyloid clusters and validated the method for different protein and dye label combinations. In particular, we studied the heparin-induced aggregation of labelled K18 tau protein *in vitro*. K18 tau comprises of the aggregation prone four-repeat domain of the tau protein, and is associated with AD and PD[4-6, 13, 27, 28]. Furthermore, we studied the aggregation of polyglutamine (polyQ) protein in HEK (human embryonic kidney) 293 cells, a protein related to HD[3, 9], large aggregates of which interfere with mitosis[10]. With the correlative FLIM - SIM experiments, we demonstrate that the lifetime sensor reports on the aggregation state of intracellular amyloid inclusions and that this offers a capability to enable high throughput screening applications.

Optical sectioning with SIM elucidates the morphology of K18 tau aggregates formed *in vitro* with sub wavelength resolution. We used the aggregation of labelled K18 tau as our *in vitro* test model for the characterization of the lifetime sensor. K18 tau monomer samples labelled with Atto 532 or Alexa Fluor® 488 at different labelling ratios (defined as the percentage of monomer peptides that were labelled with the fluorescent dyes) were prepared, and their aggregation induced by addition of heparin (see Supporting Information for details).

In order to provide reference data for the calibration of the lifetime sensor, we first characterized the morphology of K18 aggregates formed after various incubation times using SROS-SIM. SIM enables the imaging of amyloid clusters with sub-diffraction limited resolution[29, 30] without any specific requirements on the labelling ratio or photochemical properties of the fluorescent reporter dyes. SROS-SIM is furthermore particularly capable of rejecting out-of-focus light, thus greatly enhancing image contrast. Example images to demonstrate these features are shown in Figure S1 of the supporting information for clusters of K18 tau. We used a home-built SIM

system[31], and analyzed data using software developed in-house in Matlab (MathWorks[®]) (see supporting information). The SROS-SIM software incorporates a number of previously proposed algorithms[32-34] and is freely available online[35]. Image stacks were acquired by performing SROS-SIM at different focal planes through the amyloid clusters.

Figure 1 displays maximum intensity projections of 3D image stacks of representative K18-Atto532 amyloid clusters formed using varying incubation times and with labelling ratios of 5% and 30%, respectively. Clearly, fibrils were formed and assembled into loose clusters early on during the aggregation process. After *ca.* 30 hours clusters stopped growing bigger in size and instead grew into denser structures with time, before forming dense spherulite structures which did not undergo further morphological transformation in time. We estimated the average radii (radii of the smallest enclosing spheres) of the amyloid clusters to be (6.6±1.8) μm and (7.3±2.2) μm after 29.3 hours for the 5% and 30% labelled samples, respectively, and (7.5±3.4) μm and (7.0±2.1) μm for corresponding samples after 78.0 hours. Sizes and structures of both the 5% and 30% labelled amyloid clusters appeared similar for comparable incubation times, indicating that the labels did not significantly influence K18 tau aggregation for labelling ratios up to 30%. A quantitative study of the influence of different labelling ratios on aggregation kinetics is the subject of subsequent sections. However, at very high labelling ratios the influence on aggregation may become significant[36]. In Figure S2 in the Supporting Information, examples are shown for samples which were labelled at 100 % and here clear differences can be observed in the morphology of aggregates compared to those obtained at labelling ratios lower than 50%.
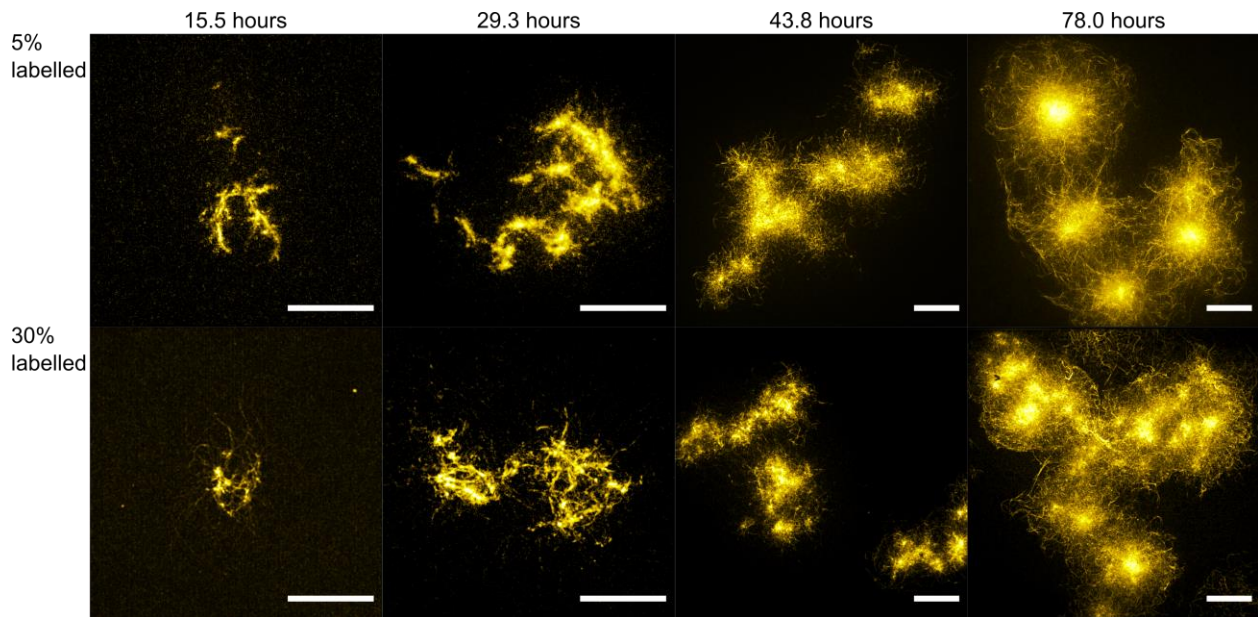
Figure 1. Maximum intensity projections of stacks of SROS-SIM super-resolution images obtained of heparin-induced K18-Atto532 amyloid clusters formed *in vitro* for different incubation times and labelling ratios. Scale bars: 10 μm.

Fluorescence self-quenching of reporter dyes informs on K18 aggregation *in vitro*. Having characterized K18 aggregate morphology with optical super-resolution microscopy, we proceeded to validate the lifetime sensor with FLIM. To begin with, we measured the lifetime of fully aggregated K18 samples labelled with different dye ratios. Fully aggregated K18-Atto532 and K18-Alexa488 samples were obtained by incubating monomer and heparin mixtures for 9 days. The samples were then imaged on a home-built TCSPC (time-correlated single photon counting) - FLIM system [15, 37, 38](also see Supporting Information), and analyzed using the FLIMfit software[39]. All data were fitted with mono-exponential decay curves (see Supporting Information). FLIM data were segmented into regions containing individual amyloid clusters which were individually analyzed. We present fluorescence lifetime values as the average value of different K18 amyloid cluster lifetimes, with error bars denoting the standard deviation.

Figure 2a and 2b show that for fully aggregated samples of K18 tau, the sensor lifetime

decreases with increasing labelling ratio, irrespective of whether Alexa 488 and Atto 532 is used

as label. For monomers we measured lifetimes of (3.689 ± 0.005) ns for K18-Atto532 and

(3.696 ± 0.002) ns for K18-Alexa488, which are higher than those corresponding to aggregates

with any labelling ratios (Figure 2a and 2b).

Potentially, the use of different labelling ratios could result in structural variations of forming

amyloid clusters, which may lead to the dyes becoming more or less buried within aggregates,

changing their solution exposure and potentially their lifetimes. To investigate potential effects

of solvent quenching, we measured the sensor lifetimes of both fully aggregated and dried

samples. Figure 2c shows the lifetime of fully aggregated samples contained in PBS, with

different Atto532 labelling ratios (yellow bars). The sample slides were then left to dry on a

heated disk of a constant temperature of 37°C. Figure 2c shows that the lifetimes of dried

amyloid clusters displayed a similar decreasing trend as the dye labelling ratio increased, even in

the absence of solvent (red bars). Finally, the samples were rehydrated again using Milli-Q®

water so that the original liquid volume was restored in the sample. The blue bars in Figure 2c

show that the sensor lifetime of the recovered samples went back to values close to those

measured before sample drying began. For all three conditions, lifetimes decreased with

increasing labelling ratios, and hence solvent effects could be excluded as the (main) cause for

the observed dependence of sensor lifetime on labelling ratio.

It had previously been speculated that the sensor lifetime decrease upon peptide aggregation may

either be due to self-quenching[23], or due to FRET like energy transfer to energy states that are

specific to amyloid structures[16, 18, 24, 37]. If the observed lifetime variation were solely due to

FRET, then increasing the dye labelling ratio would correspond to an increase in donor concentration, while the acceptor concentration (energy states of the aggregates) remains unchanged, and thus one would expect the fluorescence lifetime of the dye to increase accordingly or keep unchanged[40], which is the opposite to our observation (see Figure 2a, b). We thus hypothesized fluorescence self-quenching to be the underlying mechanism for the lifetime sensor, with peptide aggregation bringing the dye labels closer together, increasing their local concentration and thus decreasing lifetimes. Self-quenching of a dye is often described by the Stern-Volmer equation[26]:

$$\frac{\tau_0}{\tau} = \frac{I_0}{I} = 1 + f_{label}k_q\tau_0\rho \tag{1}$$

Here, τ_0 and τ represent the fluorescence lifetimes of unquenched or quenched dye, I_0 and I represent the fluorescence intensities of unquenched and quenched dyes, respectively. f_{label} is the labelling ratio of the sample, k_q is the self-quenching rate coefficient of the dye, and ρ is the local concentration of K18 peptide in the aggregate. Equation 1 was fitted to the data in Figure 2a and 2b (red line) and excellent agreement was found with the experimental data. The monomer lifetimes τ_0 recovered from the fitting are (3.68$\pm$0.04) ns for K18-Atto532 and (3.61 $\pm$0.09) ns for K18-Alexa488, similar to the corresponding values (3.689$\pm$0.005) ns and (3.696 $\pm$0.002) ns acquired experimentally. The sample corresponding to 100% dye labelling ratio was not taken into account in the fit, because these samples looked structurally different to aggregation formed using the lower labelling ratios (see Figure S2).

Next, we performed FLIM imaging experiments for K18-Atto532 amyloid clusters, using different labelling ratios and incubation times and performed a phasor plot analysis[40-43] of the FLIM data (Figure 2d for phasor plot, corresponding lifetime data shown in Figure 3a). The

phasors and error bars in Figure 2d are respectively the average values and standard deviations, calculated from the phasors of different amyloid clusters. Phasors were obtained from Fourier transform of FLIM data as reported extensively in previous work[40, 43]. The methodology makes no model assumption and provides for a powerful tool to identify and differentiate contributions from different fluorescence decay components such as FRET or self-quenching. For example, if significant energy transfer between the dyes and energy states of aggregates took place, corresponding phasor trajectories (which means phasors for samples with different incubation times) of samples with different labelling ratios would be expected to be distinct, without overlap occurring. We expect this to be true since aggregates with different structures (formed after different incubation times) are likely to feature different intrinsic energy states, and hence the FRET efficiency between dye labels and different aggregate types should be distinct. Phasors for samples with different donor and acceptor stoichiometries and different FRET efficiencies should spread over an area on the phasor plot rather than lying on the same trajectory[40]. However, as seen from Figure 2d, the phasor trajectories for different labelling ratios overlap, indicating that phasor positions are mainly related to the local dye concentrations rather than the specific type of aggregate structure forming. Figure 2e illustrates this idea schematically: the phasors for aggregates with different aggregate structure may overlap for samples with different labelling ratios, if a lower aggregate density is compensated by a higher labelling ratio and *vice versa*, leaving local dye concentrations the same. For instance, the phasors highlighted by the dashed circle in Figure 2d correspond to 20% labelled sample that was fully aggregated (red phasor) and 30% labelled sample that was in the intermediate aggregation state (blue phasor). These phasors almost overlap because the local dye densities in the amyloid clusters are similar. Taken together, these results provide firm evidence that self-quenching is the main mechanism by which the

lifetime sensor reports on aggregation. We also performed FLIM measurements for the Atto 532

- maleimide dye which we used for K18 peptide labelling, dissolved in DMSO at different

concentrations, and we verified that indeed the dye exhibits self-quenching at high concentration

(see Figure S3 in Supporting Information).
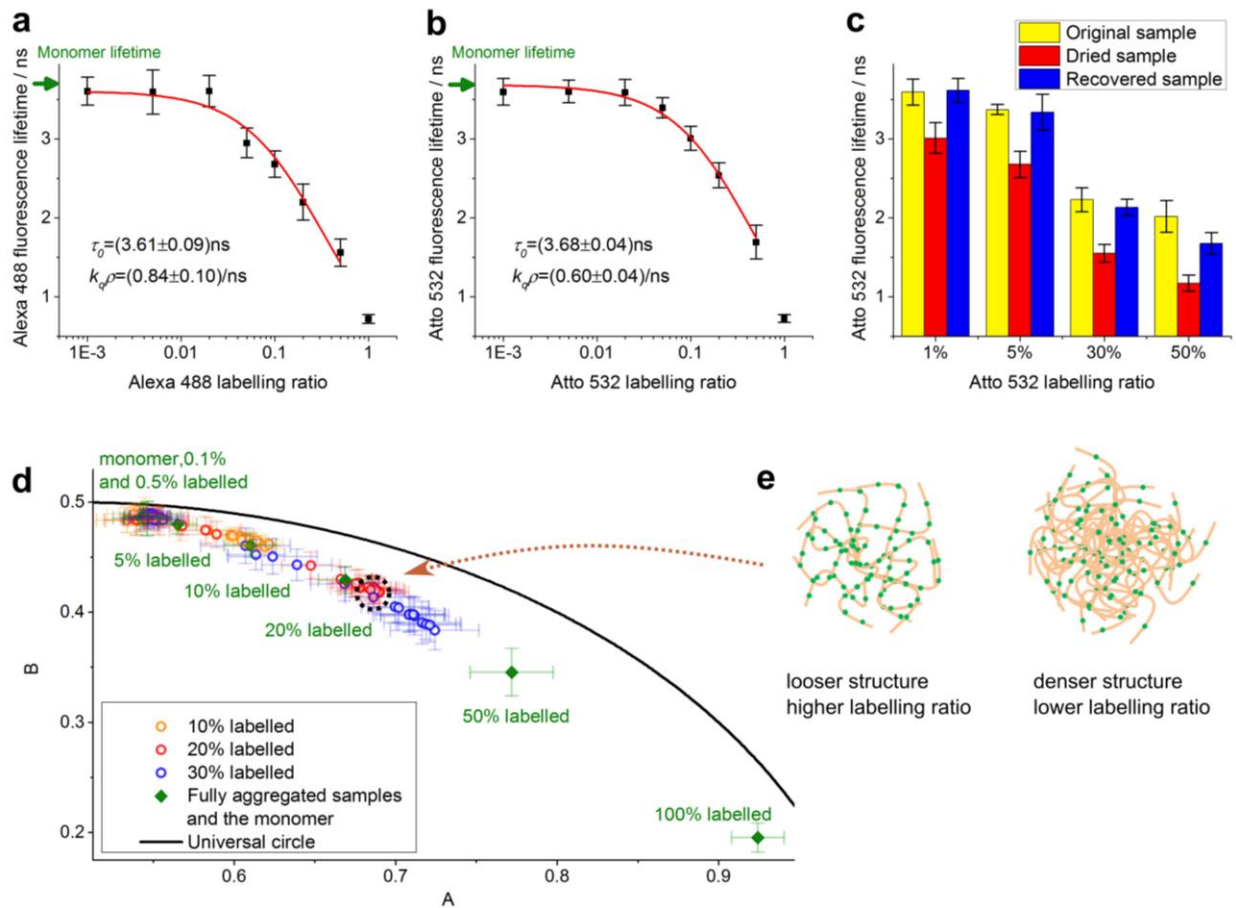
Figure 2. Fluorescence lifetime data for K18-Atto532 and K18-Alexa488 tau samples reveal

increasing degrees of fluorescence self-quenching during protein aggregation as the underlying

mechanism for lifetime changes. **a and b.** Fluorescence lifetime data and Stern-Volmer data fit

for the fully aggregated K18-Alexa488 (a) and K18-Atto532(b) samples with different labelling

ratios. **c.** Fluorescence lifetime of fully aggregated K18-Atto532 samples for different labelling

ratios in PBS solution (yellow), dried state (red), and in PBS solution after rehydration of the

10

dried state (blue). **d.** Phasor plot of FLIM data of K18-Atto532 amyloid clusters. Circles denote phasors for aggregates formed after different incubation times, with the specified labelling ratios. Solid diamonds denote phasors for monomers and fully aggregated samples with different labelling ratios, calculated from same data sets as Figure 2b. As expected, the phasors for monomer, low labelling ratio samples, and samples at early aggregation stages lie close to each other. A zoomed-in image (Figure S4) is available in the Supporting Information. **e.** Illustration to show how cluster formation with different labelling ratios can lead to overlapping phasor trajectories. Phasors overlap in those samples where the local dye concentration, and thus self-quenching, is similar; for example a more aggregated and thus denser sample with low labelling ratio (right panel) may have the same dye density as a less densely aggregated sample with high labelling ratio (left panel). Green - fluorescent dye labels; beige – proteins.

Having established that fluorescence self-quenching is the underlying mechanism behind the lifetime sensor, we went on to explore how it could be used to report on the type and nature of amyloid clusters formed under different aggregation conditions. Figure 3a shows the fluorescence lifetime data from which the phasor plot shown in Figure 2d was generated. The sensor lifetime of amyloid clusters was shown to be approximately constant for all three labelling ratios for incubation times less than approximately 30 hours. After *ca.* 30 hours the sensor lifetime began to drop and reached a bottom plateau region after approximately 55 hours of incubation. The top plateau in Figure 3a corresponds to lifetimes of (3.59 ± 0.04) ns, (3.57 ± 0.02) ns and (3.56 ± 0.02) ns for the 10%, 20% and 30% labelled samples, respectively, only *ca.* 100 ps lower than the monomer K18-Atto532 lifetime (3.689 ± 0.005) ns. We note that the SROS-SIM experiments revealed that for incubation times less than 30 hours, aggregates consisted mostly of low density clusters of loosely assembled amyloid fibrils. This suggests that

the lifetime sensor does not sensitively report on the conversion of labelled peptide into single amyloid fibrils at labelling ratios below 30% for K18. However, the sensor lifetime dropped significantly (by up to 19%, 34% and 42%, respectively, for 10%, 20%, and 30% labelled samples) during the period when the aggregate density increased. Our lifetime sensor is thus highly sensitive to fibril packing density in the amyloid cluster, rather than the formation of single fibrils. This suggests that the distance between neighboring dyes on single fibrils is not sufficiently proximate to generate significant self-quenching, whereas in clusters on the other hand, this distance drops into a highly sensitive range for dye self-quenching.

The fluorescence lifetime sensor offers a good dynamic range to report on K18 tau aggregation without significantly influencing its kinetics. Figure 3a shows that it is advantageous to use a higher labelling ratio for a larger variation in lifetime to report on aggregation. However, as mentioned previously, the aggregation kinetics and structure of amyloid clusters may be affected by very high labelling ratios (see Figure S2). A good dynamic range was obtained at 30% labelling ratio for K18 tau with lifetimes dropping by 42% from monomeric to fully aggregated state. We thus investigated the effect of peptide labelling ratio up to 30% on aggregation kinetics. Structurally the amyloid clusters formed with labelling ratios up to 30% were indistinguishable from one another, as verified by SROS-SIM calibration. In Figure 3b we show that the kinetics of aggregation are similarly unaffected and the normalized lifetime profiles overlap very well for all labelling ratios, giving support to the notion that the labelling protocols with labelling ratios below 30% had minimal effects on the aggregation processes investigated.

We developed a kinetic model to describe the *in vitro* aggregation process of K18 tau which is based on the SROS-SIM results presented above, and used it to quantify the effect of labelling on

aggregation kinetics. Figure 3c shows the model schematically. Early amyloid clusters were modelled to consist of loose assemblies of K18 tau fibrils. The amyloid clusters grow until they reach a certain size and become "mature". At this point clusters stop growing larger and instead act as "sinks" that absorb the remaining amyloid species (monomer / oligomer / fibrils) in their vicinity and thus increase in density. We assume that the number of "sinks" does not change after the amyloid clusters are "mature", and we describe the densification process of such "sinks" using the Smoluchowski sink absorption model[44-46]. Combining the Smoluchowski model and Stern-Volmer equation (Equation 1), we derived the following equation to describe K18 tau aggregation kinetics (for details of our model and derivation of this equation see Supporting Information):

$$\tau(t) = \frac{\tau_0}{1+f_{label}k_q\tau_0(\rho_{sink}(\infty)-\frac{[oligomer]_0 \cdot p}{[sink]\cdot V}\cdot e^{-\frac{4\pi DR[sink]}{1+e^{-(t-\theta)/s}}t})} \tag{2}$$

In Equation 2, τ_0 is the fluorescence lifetime of monomeric sample, and $\tau(t)$ is the average lifetime of amyloid clusters at time t. f_{label} is the labelling ratio, k_q is the self-quenching rate coefficient. $\rho_{sink}(t)$ is the average local concentration of K18 monomers inside each sink, at time t. V is the average volume of the sinks. $\frac{[oligomer]_0 \cdot p}{[sink]\cdot V}$ is a constant. $4\pi DR[sink]$ represents the K18 aggregation rate constant. θ is the average sink formation time, and s is the standard deviation of sink formation time. We perform a global fit of the aggregation kinetic data in Figure 3a using Equation 2. Results are presented in Table S1 in the Supporting Information, where a discussion of the model and demonstration of its robustness are also presented. Using global fitting for all other parameters ($k_q\rho_{sink}(\infty)$, $k_q \cdot \frac{[oligomer]_0 \cdot p}{[sink]\cdot V}$, θ and s), we were able to recover aggregation rate constants $4\pi DR[sink]$ for the 10%, 20% and 30% labelled samples as, respectively, (0.034 ± 0.006)/hour, (0.046 ± 0.010)/hour, and (0.057 ± 0.014)/hour. The average

sink formation time θ can be recovered with a similar approach and was found to be (43.0 ± 1.1), (44.6 ± 1.0) and (42.3 ± 0.9) hours for the 3 samples, respectively. Both aggregation rate constant and the average sink formation time did not vary significantly for different labelling ratios, providing firm evidence that labelling ratios up to 30% do not significantly influence the aggregation kinetics of the K18 peptide.
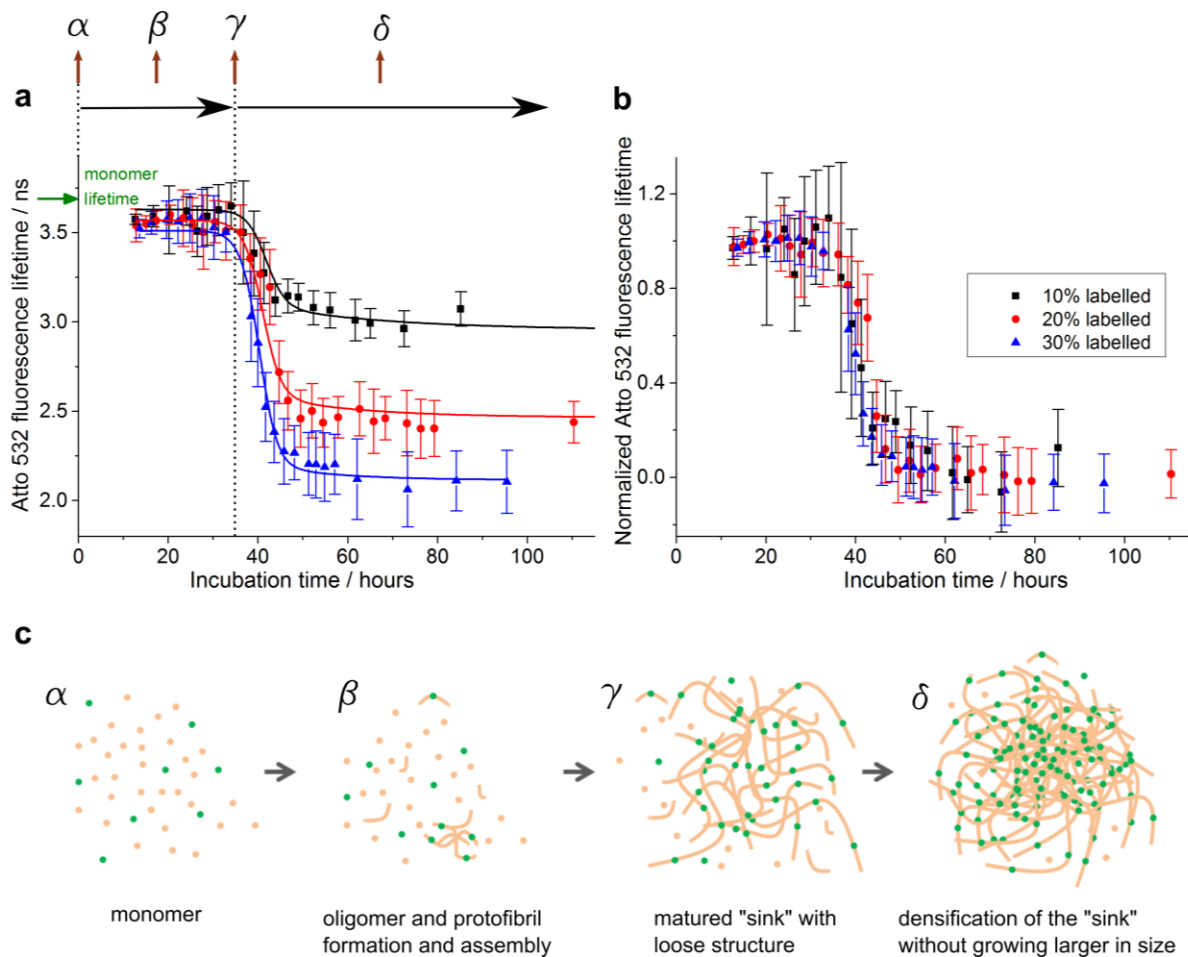
Figure 3. TCSPC-FLIM measurements of amyloid cluster formation kinetics of K18-Atto532 samples with different dye labelling ratios. **a.** Fluorescence lifetimes of K18-Atto532 as a function of aggregation time for samples with 10%, 20%, 30% labelling ratios. The sigmoidal curves are the fitted lines using the kinetic model described in the main text. **b.** Same data represented with normalized fluorescence lifetimes, demonstrating that the cluster formation

kinetics are not significantly affected by the presence of the dye labels. **c.** Schematic to illustrate the K18 tau aggregation model used for FLIM data fitting. Green - fluorescent dye labels; beige – proteins.

The fluorescence lifetime reports on the structural density of PolyQ aggresomes formed in cells. To demonstrate the lifetime sensor concept for measurement of amyloid cluster formation in cell models, we performed correlated FLIM - SIM imaging of PolyQ aggresomes formed under physiological conditions inside cells. SNAP-HDQ72-expressing HEK 293T cells were labelled with SNAP-Cell 505-Star and fixed on gridded slides[9, 10] (see Supporting Information); they were then imaged using both TCSPC-FLIM and SROS-SIM as described previously. Note that we fixed the cells only for the purpose of enabling correlative FLIM – SIM measurements, in principle the lifetime sensor can equally be applied in living cells. Figures 4d-4f show the intensity-merged FLIM images of the polyQ aggresomes, and Figures 4a-4c corresponding SROS-SIM images of the same aggresomes (animated volume renderings of the data are available in the Supporting Information). Comparing both data sets, it is seen that aggresomes with a lower lifetime display a denser structure *via* SIM and *vice versa*.

Figure 4g displays a zoomed-out FLIM image with several aggresomes appearing as bright spots (highlighted by white circles) in the same field of view. This image clearly demonstrates the high-throughput capability of the lifetime sensor. It took only *ca.* 1 minute to acquire the image on a TCSPC-FLIM system, which could be sped up further if time-gated FLIM were used instead of TCSPC[26]. The lifetime sensor reveals structural density variations between different aggresomes in a single FLIM image containing a large number of cells (see Figure 4g), providing a fast read out tool that informs on amyloid structure without requirement for imaging each cluster individually with high resolution optical microscopy or EM techniques. At the same time,

the FLIM image keeps enough spatial resolution to locate the position of the aggresomes within cells and to distinguish between aggresomes in different cells. Moreover, the lifetime provides an indication of the structural density and morphology of different amyloid clusters, whereas a similar global parameter to quantify structural density variation does not exist for high resolution methods. The lifetime sensor is thus a powerful tool for the identification of large numbers of amyloid clusters in bulk, for instance for the screening of aggresomes with different structural densities in cells or for the acquisition of statistical data of the aggresome structural densities, and such data could be further correlated with cellular phenotypes, *e.g.* a capability for cells to undergo mitosis[10].

A drawback of the lifetime sensor comes from the fact that fluorescence self-quenching is not only related to the structural properties of the amyloid clusters, but also to the labelling ratio of the sample (as shown in Figure 3a). This requires control over the labelling ratio of the sample. This can easily be achieved for *in vitro* experiments where monomer labelling ratios can be controlled, such as our K18 tau experiments shown earlier. In cell experiments, covalent bio-orthogonal labelling techniques[47, 48] such as SNAP-tag and CLIP-tag can be used to control the labelling ratios, as we have employed here for polyQ experiments in HEK cells.
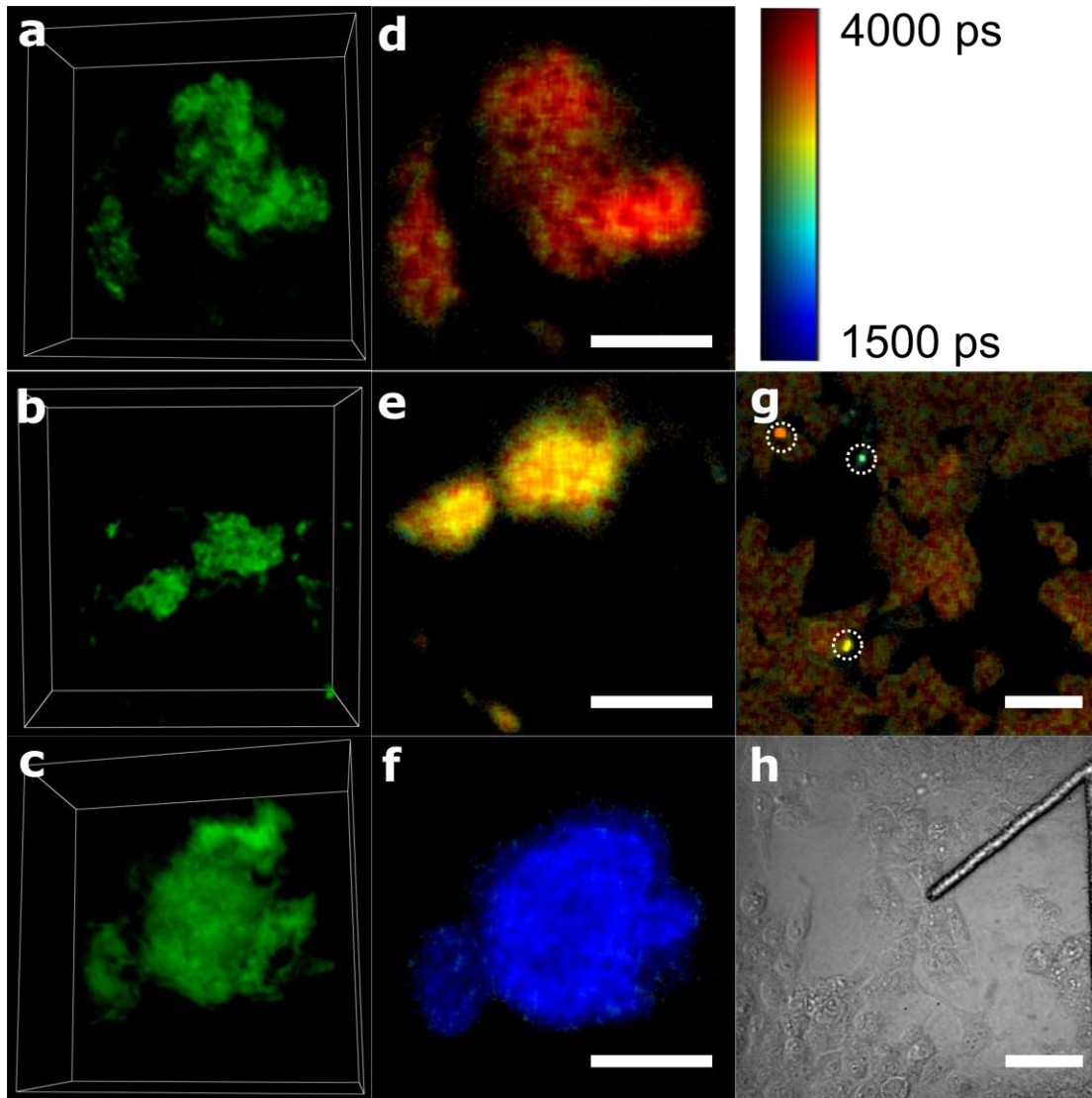
Figure 4. Correlated FLIM - SIM images of polyQ aggresomes labelled with SNAP-Cell 505-Star dye in fixed HEK cells. **a-c.** 3D images of polyQ aggresomes reconstructed from the SROS-SIM images, presented using Icy software[49]. Size for boxes in figures a-c is 15 μm×15 μm×7.1 μm. Animated 3D renderings are available in the Supporting Information. **d-f.** FLIM images of the same polyQ aggresomes corresponding to Figures a-c. Scale bar: 5 μm. **g.** FLIM image of polyQ-expressing HEK cells stained with SNAP-Cell 505-Star dye. Scale bar: 50 μm. **h.** Transmitted light image of the same field of view as the FLIM image g. The shape of

"1" is the number label on the gridded dish. The colorbar indicates the fluorescence lifetime values for figures d-f.

In summary, we present a lifetime sensor for high-throughput structural characterization of amyloid clusters both *in vitro* and in cells. Performing SROS-SIM and FLIM experiments on *in vitro* aggregated K18 tau labelled with Alexa 488 or Atto 532, we show that the lifetime sensor reports on the amyloid structural density according to the fluorescence lifetime variation of synthetic dyes covalently labelled on peptides. We demonstrate that the mechanism of the sensor is *via* fluorescence self-quenching, and that the sensor offers a good dynamic range of fluorescence lifetime variation without significantly influencing the aggregation formation. The power of lifetime sensor concept was demonstrated for cell experiments *via* correlative FLIM – SIM experiments in HEK cells on aggresomes of polyQ labelled with SNAP-Cell 505-Star. This high-throughput method allows for the screening or statistical analysis for aggresomes with different structural density formed in cells, and it can potentially be applied on studies in more physiological conditions such as brain slices *etc*.
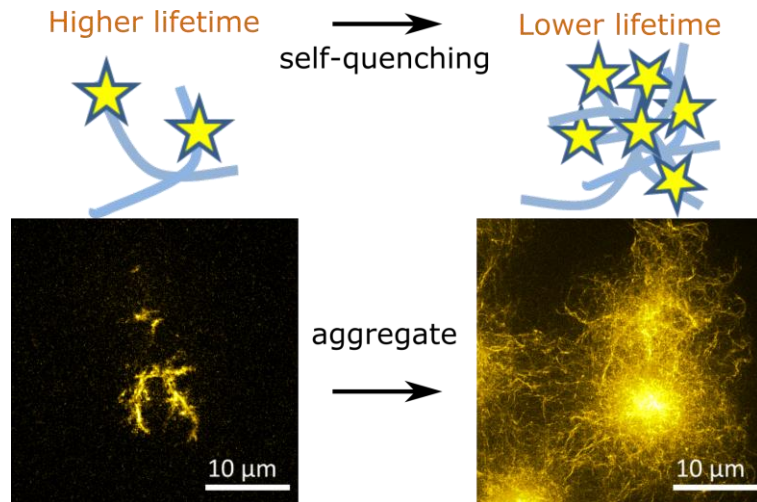
Corresponding Author

*Clemens F. Kaminski: cfk23@cam.ac.uk;

Table of Contents graphic

Supporting Information Available:

Details of the sample preparation, imaging parameters, data analysis, the fitting results and discussions of the K18 aggregation kinetics data, and the supporting figures are available in the .docx file. Animated 3D renderings corresponding to Figure 4a-c are presented in the .avi files.

This material is available free of charge via the Internet at http://pubs.acs.org.

REFERENCES

(1)   Ciryam, P.; Tartaglia, G. G.; Morimoto, R. I.; Dobson, C. M.; Vendruscolo, M. *Cell Rep.* **2013**, *5*, 781–790.

(2)   Sipe, J. D.; Cohen, A. S. *J. Struct. Biol.* **2000**, *130*, 88–98.

(3)   Bates, G. *The Lancet* **2003**, *361*, 1642–1644.

(4)   Aguzzi, A.; O'Connor, T. *Nat. Rev. Drug Discovery* **2010**, *9*, 237–248.

(5)   Stefani, M.; Dobson, C. M. *J. Mol. Med.* **2003**, *81*, 678–699.

(6)   Selkoe, D. J. *Nat. Cell Biol.* **2004**, *6*, 1054–1061.

(7)   Bacskai, B. J.; Skoch, J.; Hickey, G. A.; Allen, R.; Hyman, B. T. *J. Biomed. Opt.* **2003**, *8*, 368–375.

(8)   Kollmer, M. et al. *Proc. Natl. Acad. Sci.* **2016**, *113*, 5604–5609.

(9)   Lu, M.; Williamson, N.; Boschetti, C.; Ellis, T.; Yoshimi, T.; Tunnacliffe, A. *Biotechnol. Bioeng.* **2015**, *112*, 1883–1892.

(10)   Lu, M.; Boschetti, C.; Tunnacliffe, A. *J. Biol. Chem.* **2015**, *290*, 27986–28000.

(11)   Guo, S.; Akhremitchev, B. B. *Biomacromolecules* **2006**, *7*, 1630–1636.

(12)   Stine Jr, W.; Snyder, S.; Ladror, U.; Wade, W.; Miller, M.; Perun, T.; Holzman, T.; Krafft, G. *J. Protein Chem.* **1996**, *15*, 193–203.

(13)   Mukrasch, M. D.; Biernat, J.; von Bergen, M.; Griesinger, C.; Mandelkow, E.; Zweckstetter, M. *J. Biol. Chem.* **2005**, *280*, 24978–24986.

(14)   Roberti, M. J.; Bertoncini, C. W.; Klement, R.; Jares-Erijman, E. A.; Jovin, T. M. *Nat. Methods* **2007**, *4*, 345–351.

(15)   Chan, F. T.; Kaminski Schierle, G. S.; Kumita, J. R.; Bertoncini, C. W.; Dobson, C. M.; Kaminski, C. F. *Analyst* **2013**, *138*, 2156–2162.

(16)   Pinotsi, D.; Grisanti, L.; Mahou, P.; Gebauer, R.; Kaminski, C. F.; Hassanali, A.; Kaminski Schierle, G. S. *J. Am. Chem. Soc.* **2016**, *138*, 3046–3057.

(17)   Ries, J.; Udayar, V.; Soragni, A.; Hornemann, S.; Nilsson, K. P. R.; Riek, R.; Hock, C.;

Ewers, H.; Aguzzi, A. A.; Rajendran, L. *ACS Chem. Neurosci.* **2013**, *4*, 1057–1061.

(18)   Esbjörner, E. K.; Chan, F.; Rees, E.; Erdelyi, M.; Luheshi, L. M.; Bertoncini, C. W.;

Kaminski, C. F.; Dobson, C. M.; Kaminski Schierle, G. S. *Chem. biol.* **2014**, *21*, 732–742.

(19)   Kaminski Schierle, G. S.; Van De Linde, S.; Erdelyi, M.; Esbjörner, E. K.; Klein, T.;

Rees, E.; Bertoncini, C. W.; Dobson, C. M.; Sauer, M.; Kaminski, C. F. *J. Am. Chem. Soc.* **2011**,

133, 12902–12905.

(20)   Pinotsi, D.; Buell, A. K.; Galvagnion, C.; Dobson, C. M.; Kaminski Schierle, G. S.;

Kaminski, C. F. *Nano Lett.* **2014**, *14*, 339–345.

(21)   Laine, R. F.; Schierle, G. S. K.; van de Linde, S.; Kaminski, C. F. *Methods Appl.

Fluoresc.* **2016**, *4*, 022004.

(22)   Kaminski, C. F.; Kaminski Schierle, G. S. *Neurophotonics* **2016**, *3*, 041807.

(23)   Quinn, S. D.; Dalgarno, P. A.; Cameron, R. T.; Hedley, G. J.; Hacker, C.; Lucocq, J. M.;

Baillie, G. S.; Samuel, I. D.; Penedo, J. C. *Mol. BioSyst.* **2014**, *10,* 34–44.

(24)   Michel, C. H.; Kumar, S.; Pinotsi, D.; Tunnacliffe, A.; George-Hyslop, P. S.;

Mandelkow, E.; Mandelkow, E.-M.; Kaminski, C. F.; Schierle, G. S. K. *J. Biol. Chem.* **2014**, *289*,

956–967.

(25)   McGinty, J.; Taylor, H. B.; Chen, L.; Bugeon, L.; Lamb, J. R.; Dallman, M. J.;

French, P. M. *Biomed. Opt. Express* **2011**, *2*, 1340–1350.

(26)   Lakowicz, J. R. *Principles of fluorescence spectroscopy*; Springer US, 2013.

(27)   Shammas, S. L.; Garcia, G. A.; Kumar, S.; Kjaergaard, M.; Horrocks, M. H.; Shivji, N.;

Mandelkow, E.; Knowles, T. P.; Mandelkow, E.; Klenerman, D. *Nat. Commun.* **2015**, *6*.

(28)   Ballatore, C.; Lee, V. M.-Y.; Trojanowski, J. Q. *Nat. Rev. Neurosci.* **2007**, *8*, 663–672.

(29)   Ströhl, F.; Kaminski, C. F. *Optica* **2016**, *3*, 667–677.

(30)   Gustafsson, M. G. *J. Microsc.* **2000**, *198*, 82–87.

(31)   Young, L. J.; Ströhl, F.; Kaminski, C. F. *J. Vis. Exp.* **2016**, *111*, e53988.

(32)   Gustafsson, M. G.; Shao, L.; Carlton, P. M.; Wang, C. R.; Golubovskaya, I. N.;

Cande, W. Z.; Agard, D. A.; Sedat, J. W. *Biophys. J.* **2008**, *94*, 4957–4970.

(33)   Wicker, K. *Opt. Express* **2013**, *21*, 24692–24701.

(34)   Shaw, M.; Zajiczek, L.; O'Holleran, K. *Methods* **2015**, *88*, 11–19.

(35)   *The SROS-SIM software is freely available online via laser.ceb.cam.ac.uk.*

(36)   Amaro, M.; Wellbrock, T.; Birch, D. J.; Rolinski, O. J. *Applied Physics Letters* **2014**, *104*,
063704.

(37)   Kaminski Schierle, G. S.; Bertoncini, C. W.; Chan, F. T. S.; van der Goot, A. T.;

Schwedler, S.; Skepper, J.; Schlachter, S.; van Ham, T.; Esposito, A.; Kumita, J. R.; Nollen, E.

A. A.; Dobson, C. M.; Kaminski, C. F. *ChemPhysChem* **2011**, *12*, 673–680.

(38)   Frank, J.; Elder, A.; Swartling, J.; Venkitaraman, A.; Jeyasekharan, A.; Kaminski, C. *J.
Microsc.* **2007**, *227*, 203–215.

(39)   Warren, S. C.; Margineanu, A.; Alibhai, D.; Kelly, D. J.; Talbot, C.; Alexandrov, Y.; Munro, I.; Katan, M.; Dunsby, C.; French, P. M. *PLoS One* **2013**, *8*, e70687.

(40)   Chen, W.; Avezov, E.; Schlachter, S. C.; Gielen, F.; Laine, R. F.; Harding, H. P.; Hollfelder, F.; Ron, D.; Kaminski, C. F. *Biophys. J.* **2015**, *108*, 999–1002.

(41)   Digman, M. A.; Caiolfa, V. R.; Zamai, M.; Gratton, E. *Biophys. J.* **2008**, *94*, L14–L16.

(42)   Redford, G. I.; Clegg, R. M. *J. Fluoresc.* **2005**, *15*, 805–815.

(43)   Clayton, A.; Hanley, Q.; Verveer, P. *J. Microsc.* **2004**, *213*, 1–5.

(44)   Von Smoluchowski, M. *Zeitschrift für physikalische Chemie* **1917**, *92*, 129–168.

(45)   Rice, S. A. *Diffusion-limited reactions*; Elsevier, 1985; Vol. 25.

(46)   Dorsaz, N.; De Michele, C.; Piazza, F.; De Los Rios, P.; Foffi, G. *Phys. Rev. Lett.* **2010**, *105*, 120601.

(47)   Dean, K. M.; Palmer, A. E. *Nat. Chem. Biol.* **2014**, *10*, 512–523.

(48)   McKay, C. S.; Finn, M. *Chemistry & biology* **2014**, *21*, 1075–1101.

(49)   de Chaumont, F.; Dallongeville, S.; Chenouard, N.; Hervé, N.; Pop, S.; Provoost, T.; Meas-Yedid, V.; Pankajakshan, P.; Lecomte, T.; Le Montagner, Y.; Lagache, T.; Dufour, A.; Olivo-Marin, J.-C. *Nat. Methods* **2012**, *9*, 690–696.